

LMSeg: A deep graph message-passing network for efficient and accurate semantic segmentation of large-scale 3D landscape meshes

Zexian Huang^{a,*}, Kourosh Khoshelham^a, Gunditj Mirring Traditional Owners Corporation^b, Martin Tomko^a

^aThe University of Melbourne, Parkville, 3010, Victoria, Australia

^bGunditj Mirring Traditional Owners Corporation, 248 Condah Estate Road, Breakaway Creek, 3303, Victoria, Australia

Abstract

Semantic segmentation of large-scale 3D landscape meshes is pivotal for various geospatial applications, including spatial analysis, automatic mapping and localization of target objects, and urban planning and development. This requires an efficient and accurate 3D perception system to understand and analyze real-world environments. However, traditional mesh segmentation methods face challenges in accurately segmenting small objects and maintaining computational efficiency due to the complexity and large size of 3D landscape mesh datasets. This paper presents an end-to-end deep graph message-passing network, LMSeg, designed to efficiently and accurately perform semantic segmentation on large-scale 3D landscape meshes. The proposed approach takes the barycentric dual graph of meshes as inputs and applies deep message-passing neural networks to hierarchically capture the geometric and spatial features from the barycentric graph structures and learn intricate semantic information from textured meshes. The hierarchical and local pooling of the barycentric graph, along with the effective geometry aggregation modules of LMSeg, enable fast inference and accurate segmentation of small-sized and irregular mesh objects in various complex landscapes. Extensive experiments on two benchmark datasets (natural and urban landscapes) demonstrate that LMSeg significantly outperforms existing learning-based segmentation methods in terms of object segmentation accuracy and computational efficiency. Furthermore, our method exhibits strong generalization capabilities across diverse landscapes and demonstrates robust resilience against varying mesh densities and landscape topologies.

Keywords: Semantic segmentation, Message-passing neural network, 3D landscape meshes, Barycentric dual graph, End-to-end architecture

1. Introduction

Recent advancements in data acquisition and terrain reconstruction methods enabled efficient, automated modelling of large-scale landscape terrains. Modelling of landscapes relies on the representation of the terrain and potential spatial objects on the terrain as 2.5D rasters (regularly-spaced cells with elevation), or as textured 3D meshes of irregular triangles. Compared to 3D point cloud or 2.5D raster landscape representations, 3D mesh modelling of landscapes *explicitly* capture geometric information and semantic attributes (e.g., texture/landcover, aspect, gradient) associated with triangle surfaces encoding explicit face adjacency. Current 3D mesh *segmentation* methods are, however, still underdeveloped and underused compared to raster segmentation, and are facing significant challenges with: (1) the accuracy of segmentation, especially on small objects; (2) the tractability and efficiency of computation (i.e, efficient model training and inference); and with (3) evaluation on diverse, large-scale landscape mesh datasets, as discussed in a recent survey (Adam et al., 2023). These challenges explicitly point out the

ongoing problems in existing landscape segmentation models, suggesting limited accuracy in segmenting complex terrain structures and high computational complexity that limits the model applications to large-scale landscape mesh datasets (Kölle et al., 2021; Gao et al., 2021). With the segmentation accuracy and efficiency issues, we pose the following question: *How to improve the accuracy and efficiency of mesh segmentation by leveraging the geometric (i.e., face normals and Euclidean coordinates) and semantic (i.e., RGB or HSV color) information of large-scale landscape meshes?* We hypothesize that the barycentric dual graph representation of landscape meshes can tightly capture the rich semantic and informative topography of mesh surfaces, which enable end-to-end model trainability with graph-based learning architectures (Gilmer et al., 2017) and facilitate expressive feature learning for accurate and efficient landscape segmentation.

We propose an accurate and efficient deep network architecture, **Landscape Mesh Segmentation Network (LMSeg)**, for semantic segmentation of large-scale high-resolution 3D landscape mesh data. LMSeg takes as input the barycentric dual of triangle meshes (i.e., the barycentric dual graph) constructed from irregular 3D point clouds as Triangular Irregular Networks (TINs). We append geometric features of the TIN (i.e., face normals and Euclidean point coordinates) and/or overlaid semantic features (e.g., HSV or RGB colour) of the triangle mesh

*Corresponding author

Email addresses: zexianh@student.unimelb.edu.au (Zexian Huang), k.khoshelham@unimelb.edu.au (Kourosh Khoshelham), reception@gunditjmirring.com (Gunditj Mirring Traditional Owners Corporation), tomkom@unimelb.edu.au (Martin Tomko)

as node features of the barycentric dual graph for model learning, without requiring additional hand-crafted mesh features as in previous methods (Rouhani et al., 2017; Gao et al., 2021; Weixiao et al., 2023). The barycentric dual graph captures the topological information of the primal mesh (i.e., explicit face adjacency) in the barycentric graph *edges*, and carries the geometric and semantic information of mesh faces as attributes of the barycentric graph *nodes* (Milano et al., 2020; Yang et al., 2023). This is to enable the encoding of information attached to areas (triangle faces) to a single node, facilitating the integration with current standard graph-based learning architectures and efficient end-to-end trainability (learning) and inference on the resulting barycentric graph.

LMSeg’s **segmentation accuracy** is grounded in its ability to hierarchically and adaptively learn local latent geometric embedding from the input barycentric dual graph. We propose an effective *geometry aggregation+* (**GA+**) module that supports hierarchical learning of expressive local geometric latent embedding via positional embedding and adaptive feature aggregation. **Efficient computation** is achieved through random node sub-sampling and heuristic edge similarity pooling to hierarchically sub-sample (reduce) barycentric dual graphs of the landscape mesh.

We evaluate the proposed LMSeg segmentation model on a large-scale public urban mesh dataset SUM (Gao et al., 2021). LMSeg model achieves a higher accuracy, 73.0% mIoU and 79.8% mAcc. at fast inference time in comparison with existing learning-based segmentation methods. We further test the segmentation performance of LMSeg on a natural landscape mesh dataset generated from high-resolution georeferenced lidar point clouds data covering the Budj Bim National Park in Victoria, Australia (Budj Bim Wall (BBW) dataset). On the BBW dataset, LMSeg exhibits strong performance with 59.5% mIoU and 74.6% F1 score for the segmentation of irregular stone wall structures under real-world, natural landscape conditions (with variable vegetation occlusion). Further ablation study of LMSeg suggests that the geometric (i.e., face normals) and semantic features (e.g., HSV or RGB colour) of triangle meshes are crucial input features, which variably impact the segmentation performance of learning models at both datasets.

2. Background

2.1. Surface Representations and Segmentation

The segmentation of landscape surfaces (with or without 3D objects) has been the subject of significant interest in the spatial sciences. Extensive studies have conducted on semantic segmentation of real-world large-scale landscapes, increasingly at fine resolutions (Blaschke, 2010). Three dominant methods exist for the representation of such landscapes: (1) directly measured irregularly (cloud) or regular (grid) sets of georeferenced points capturing 3D coordinates of point locations on a surface; (2) regular cell-based georeferenced raster representations of aggregate (typically, mean) elevation values in the area covered by a cell, or (3) mesh representations of Triangular Irregular Networks (TIN) of terrains Peucker et al. (1976). Typically, lidar-based

unstructured point clouds are transformed, via interpolation to raster representations, or by meshing to TINs. Meshed TINs therefore typically include all (or a subset of) measured point cloud data, but construct a digital model of a surface where the top/bottom orientation of a face (normal) can be captured (see Section 3.1).

In raster-based landscape segmentation, deep learning methods usually leverage convolutional neural networks (CNN) (He et al., 2016; Girshick et al., 2014) to learn deep semantic features for input images and classify image pixels to semantic labels. CNNs are commonly applied to raster-based surface segmentation, due to the problem’s equivalence to image analysis, for which CNNs were developed. A recent method from Wang et al. (2022) applied the Vision Transformer (ViT) architecture (Dosovitskiy et al., 2020) for semantic segmentation of remote sensing imagery and achieved state-of-art segmentation accuracy. However, the 2D imagery segmentation methods can not effectively solve the object occlusion problem in 2D imagery domain.

When applied to 3D point cloud segmentation of landscapes, point-based (Qi et al., 2017a,b; Tailor et al., 2021; Zhao et al., 2021; Hu et al., 2020; Thomas et al., 2019) and graph-based methods (Wang et al., 2019; Li et al., 2019; Landrieu and Simonovsky, 2018) have demonstrated the importance of learning local geometric point features from locally grouped neighbours (to construct the graphs) for point clouds analysis (e.g., classification and segmentation tasks) and graph-structure learning (e.g., node and graph classifications). These 3D point cloud segmentation methods (Qi et al., 2017a,b; Landrieu and Simonovsky, 2018; Hu et al., 2020; Thomas et al., 2019) rarely utilise additional geometric and semantic point features (i.e., point normals and texture information) for landscape segmentation due to the lack of diverse point features provided in landscape datasets.

2.2. Mesh-based Surface Segmentation

In contrast to the landscape surface segmentation on 2D rasters and 3D point clouds, triangular mesh segmentation models assign a semantic label from a set of semantic classes directly to input 3D TIN mesh faces (possibly attributed with auxiliary input features) (Gao et al., 2021; Adam et al., 2023). Most of these models are most commonly applied 3D models of objects, rather than to landscape surfaces.

The mesh-based model by Rouhani et al. (2017) partitions textured meshes into superfacets by a region growing approach based on geometric similarity measures of triangle facets, then computes a set of geometric and photometric features for each superfacet. A random decision tree classifier is then trained on hand-crafted features, and a Markov Random Field predicts corresponding semantic labels for each superfacet. Following this work, SUM-RF from Gao et al. (2021) proposed a semi-automatic annotation method for labelling a large-scale urban landscape mesh dataset, which includes an initial segmentation stage that over-segments input meshes into superfacets and trains a random forest classifier based on hand-crafted features of superfacets for automatic mesh labelling. While these approaches (Rouhani et al., 2017; Gao et al., 2021) achieve stable segmentation performance on large-scale landscape mesh datasets, they require additional hand-crafting mesh features (i.e., geometric

and radiometric features) based on over-segmented mesh superfacts for subsequent learning tasks, which inhibits end-to-end model trainability.

Hanocka et al. (2019) propose MeshCNN, an intrinsic mesh model that applies deep convolution and pooling directly on mesh edges. Extensions of MeshCNN, MeshNet (Feng et al., 2019) and MeshNet++ (Singh et al., 2021) take mesh faces as inputs to spatial and structural descriptors and generate a set of initial spatial and structural mesh features, on which a mesh convolution network is then trained for classification and retrieval tasks. A different approach by Tang and Qiu (2021) converts 3D meshes into graph data and aggregates the spatial and structural mesh features from the local neighborhoods of graph nodes with a densely connected graph convolution network (Kipf and Welling, 2017) for object part segmentation. Guan et al. (2021) transforms 3D meshes into barycentric point sets and construct dual local graphs, and apply a local-global combined point-based network for object part segmentation. While the methods discussed above attain end-to-end model trainability, they are mostly tested on small-scale synthetic 3D mesh data (i.e., clean and hand-crafted manifold meshes: cubes, spheres and torus, or models of toys) (Bronstein et al., 2011; Wu et al., 2015; Hanocka et al., 2019) and are rarely tested on large-scale non-manifold georeferenced landscape meshes (i.e., 2.5D surfaces), possibly suffering from incompleteness (gaps), and containing defects and noise.

2.3. Learning Models for Urban Meshes

To evaluate mesh segmentation and scene understanding methods on real-world landscape mesh data, a learning-based approach by Tutzauer et al. (2019) computes the barycenter of landscape surface mesh triangles as point clouds. A multi-branch 1D CNN network is trained on the geometric and radiometric features of point clouds (i.e., the barycenter of landscape meshes) to predict per-face labels. Later, Laupheimer et al. (2020) associated 3D lidar point clouds with textured meshes and apply a PointNet++ (Qi et al., 2017b) for mesh segmentation. The method by Tang et al. (2022) abstracts the triangular meshes into the barycentric point clouds of meshes and applies a point-based Transformer architecture (Zhao et al., 2021) for downstream mesh segmentation. However, the point-based transformer learning architecture (Zhao et al., 2021) in Tang et al. (2022) is comparatively computationally expensive and requires over 40 hours of training time on a proprietary urban dataset for mesh segmentation, which significantly limits the model applicability for larger mesh datasets. The approach proposed by Yang et al. (2023) represents the triangle meshes of landscape as surface graphs (i.e., barycentric dual graphs) and then applies a hierarchical deep network for mesh segmentation. This approach resembles a point-based segmentation architecture (Qi et al., 2017b) and hierarchically constructs surface connective neighbourhoods (SC neighborhood) of barycentric dual graphs for hierarchical feature learning on input meshes. Additional TextureConv blocks based on 2D convolution networks are required to learn facet texture features on the textures of triangle meshes for semantic segmentation but limits the end-to-end trainability of proposed model. PSSNet by Weixiao et al. (2023) proposed

a two-stage deep learning-based architecture for urban mesh segmentation, where the geometric node and edge features are extracted by deep neural networks for superfacet classification. The two-stage PSSNet learning architecture requires a super-point grouping and edge dependency extraction process in the first stage for the subsequent model learning in the second stage. This model design fails to jointly optimise the two-stage model architecture and therefore is prohibitive to end-to-end model trainability and causing inefficient model inference.

3. Methodology

In this section, we introduce the building blocks of LMSeg, a deep message-passing network proposed for efficient and accurate large-scale landscape mesh segmentation tasks. First, in Section 3.1 we provide the formal definition of the barycentric dual graph input used by LMSeg, encoding the landscape surface mesh representation for learning and inference. The overall network architecture of LMSeg is then described in Section 3.2. Section 3.3 presents the **Geometry Aggregation+** (GA+) module providing an effective geometry aggregation to LMSeg, which adaptively learns geometric latent embeddings on the barycentric dual graph $\mathcal{G}(\mathcal{M})$. Section 3.4 then discusses the efficient hierarchical node sub-sampling and local edge pooling method of LMSeg.

3.1. Triangular Mesh and its Barycentric Dual Graph

Consider a landscape surface \mathcal{S} represented as a triangular mesh $\mathcal{M} = (\mathcal{V}, \mathcal{E}, \mathcal{F})$, where $\mathcal{V} \in \mathbb{R}^{N \times 3}$ is a set of unordered points captured by their spatial coordinates on \mathcal{S} (therefore $\mathcal{V} \in \mathcal{S}$), $\mathcal{E} \in \mathbb{R}^{N \times N}$ is a matrix of edge indices $\mathcal{E} \subseteq \mathcal{V} \times \mathcal{V}$, which denotes a set of undirected edges that connect nodes in \mathcal{V} , $\mathcal{F} = \{(i, j, k) \in \mathcal{V}\}$ is a set of ordered triplets constituting the triangle faces of the mesh. Together, nodes \mathcal{V} , edges \mathcal{E} and faces \mathcal{F} form a 3D mesh model capturing the geometry of the surface (terrain and potential 3D objects) in real-world environments (Peucker et al., 1976; Adam et al., 2023).

The triangle mesh \mathcal{M} is converted into its topological dual, the barycentric graph \mathcal{G} . Concretely, an undirected barycentric graph $\mathcal{G}(\mathcal{M})$ represents a triangular surface mesh as a node \mathcal{V} matrix of the spatial coordinates of barycenters of the triangular mesh faces $\mathcal{F} \in \mathcal{M}$ and an edge \mathcal{E} matrix capturing the face adjacency $\mathcal{E} \subseteq \mathcal{F}_{\mathcal{M}} \times \mathcal{F}_{\mathcal{M}}$. An additional node feature matrix $\mathcal{X} \in \mathbb{R}^{N \times C}$ encodes the corresponding face features (i.e., attributes) from \mathcal{M} (e.g., face normals and texture information).

3.2. Network Architecture

We present the overall network architecture of LMSeg in Fig. 1, which shares a encoder-decoder network architecture as Qi et al. (2017b).

Inputs: the node features \mathcal{X} (i.e., mesh textures and face normals) and coordinates \mathcal{V} of the barycentric graph $\mathcal{G}(\mathcal{M})$ are passed to a multilayer perceptron (MLP) layer to generate the latent node embedding of input features. The latent node embedding along with the initial edge matrix \mathcal{E} of $\mathcal{G}(\mathcal{M})$ is passed

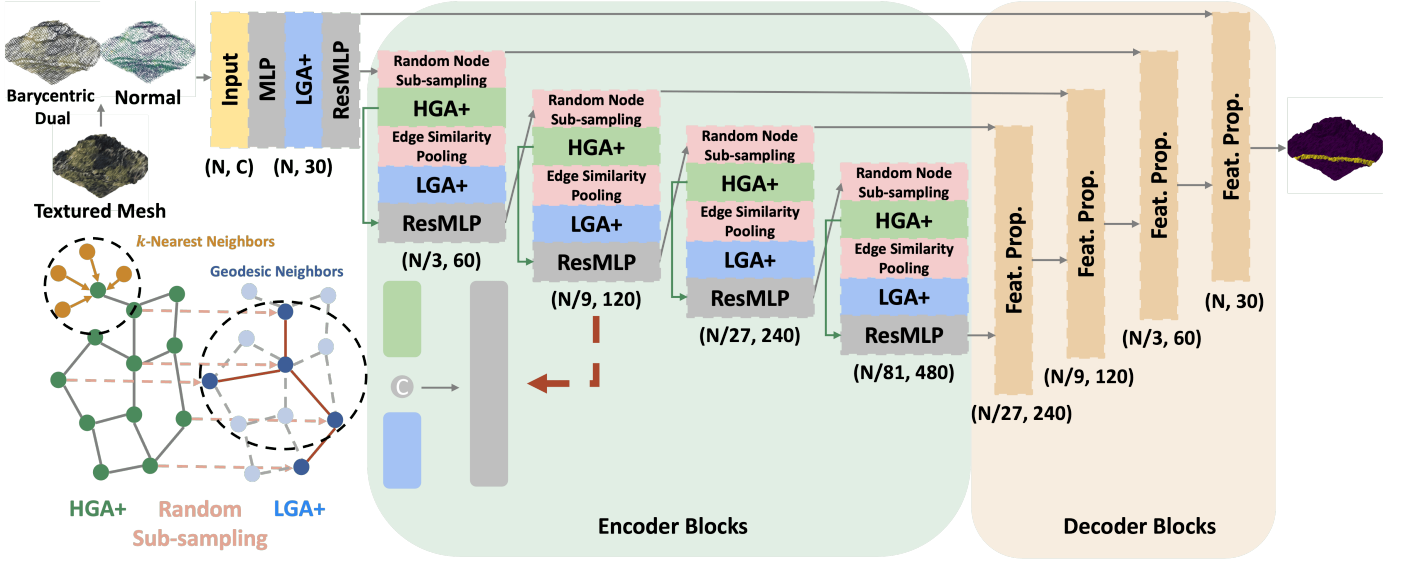


Figure 1: Overall architecture of LMSeg. (a). Input mesh is converted into barycentric dual graph with mesh texture and face normal features. (b). LMSeg encoder consists of random node sub-sampling, HGA+, edge pooling and LGA+ modules for hierarchical and local feature learning. A residual MLP takes concatenated LGA+ and HGA+ features as inputs and updates graph node features. (c). LMSeg decoder consists of feature propagation layers, which progressively up-sample the size of deep encoder features back to the original input size. N denotes the number of input nodes of barycentric dual graph, and C refers to the input node feature dimensions.

to a GA+ module (Sec. 3.3) to learn local geometric features capturing the high-frequency details of the 3D geometry of the surface.

Encoder.: the latent node embedding of GA+ module from inputs enter the encoder blocks, as displayed in Fig.1, following the sequence: random node sub-sampling \rightarrow hierarchical geometry aggregation+ (HGA+) \rightarrow edge similarity pooling \rightarrow local geometry aggregation+ (LGA+) \rightarrow residual MLP (ResMLP). The latent node embedding of HGA+ and LGA+ modules in each encoder block are concatenated as dense features and passed to the ResMLP layer to learn deep latent features with residual connections (He et al., 2016; Ma et al., 2022). Overall, each encoder block downsamples the vertex number of $\mathcal{G}(\mathcal{M})$ by 1/3 hierarchically with the random node sub-sampling and doubles the feature dimensions of latent node embedding of $\mathcal{G}(\mathcal{M})$ with the ResMLP layer.

Decoder.: a symmetric decoder design is implemented, following the pattern established by point-based learning networks (Qi et al., 2017b; Qian et al., 2022). The symmetric decoder progressively up-samples the size of deep encoder features back to the original input size. In each decoder block, the feature propagation layer interpolates the abstract features of the input encoder feature at layer l based on inverse distance weighted average and k -nearest neighbors ($k=3$). The abstract features are added to the homologous encoder features from layer $l-1$ and passed to an MLP layer.

3.3. Geometry Aggregation Module GA+

GA+ modules are the main feature learning components in LMSeg encoder, as displayed in Fig.2, which is a graph message-passing network consists of geometric feature learning of local

graph neighbourhoods, incorporation of positional embedding to local geometric features and the learnable feature aggregation.

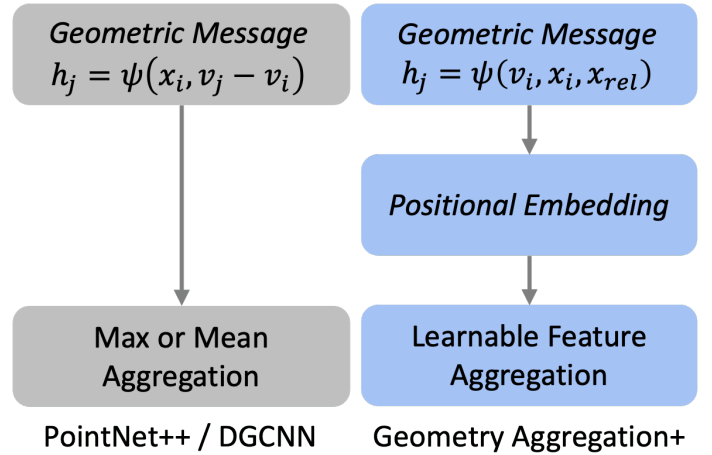


Figure 2: Different graph message-passing networks adopted in the geometry aggregation+ (GA+) module and typical point-based / graph-based learning approaches (Qi et al., 2017b; Wang et al., 2019).

Graph message-passing convolution.: The aim of the GA+ module learns a local geometric latent embedding via graph message-passing convolution. Following the generic recipes of (Qi et al., 2017b; Tailor et al., 2021; Zhao et al., 2021), the local geometric latent embedding of $\mathcal{G}(\mathcal{M})$ is learned as:

$$\mathbf{h}_j = \psi(\mathbf{v}_i, \mathbf{x}_i, \mathbf{x}_{rel}), \quad (1)$$

where ψ denotes a learnable function (i.e., shared MLPs), $\mathbf{x}_i \in \mathcal{X}$ are the input mesh features (i.e., face normals and texture information) of the target node $\mathbf{v}_i \in \mathcal{V}$, and $\mathbf{x}_{rel} = \frac{(\mathbf{x}_j - \mathbf{x}_i)}{\sigma + \epsilon}$, $\mathbf{x}_j \in \mathcal{X}_{\mathcal{K}_i}$

is the normalised relative node feature between the source and target node features in an undirected local graph neighbourhood grouped by edges \mathcal{E} or a k -nearest neighbors (k -NN) function. In the normalised relative node features, the σ represents the standard deviation of relative node features and ϵ is a small value (i.e., $1e^{-5}$) for numerical stability (Ma et al., 2022).

Positional Embedding: As pointed out by Tancik et al. (2020); Zhang et al. (2023), the positional embedding using trigonometric functions in Transformer-based (Vaswani et al., 2017) models for 3D point cloud learning is commonly applied for describing the position of an entity in a sequence and enables MLPs capturing the high-frequency latent embedding and fine-grained details of 3D structures in low dimensional domains. As the barycentric graph $\mathcal{G}(\mathcal{M})$ of triangle mesh encodes both the topology (by edges \mathcal{E}) and geometric information (by nodes \mathcal{V}), the high-frequency spatial structures of $\mathcal{G}(\mathcal{M})$ can be effectively captured by transforming low-dimensional Euclidean inputs (i.e., $\mathbf{v} \in \mathcal{V}$) to high-dimensional positional embeddings:

$$\begin{aligned} PE(\mathbf{v}_{rel}, 2c) &= \mathbf{sin}(\alpha * \mathbf{v}_j / \beta^{(2c/d)}), \\ PE(\mathbf{v}_{rel}, 2c + 1) &= \mathbf{cos}(\alpha * \mathbf{v}_j / \beta^{(2c/d)}), \end{aligned} \quad (2)$$

where $\mathbf{v}_{rel} = (\mathbf{v}_j - \mathbf{v}_i)$ is the relative spatial position of the source and target nodes, α ($=100$) controls the granularity of the positions (i.e., the level of fine-grained changes in vertex positions), β ($=1000$) is the base frequency of sinusoidal functions, c refers to the input channels and d is the output dimensions of positional embedding vector $PE(\mathbf{v}_j)$.

The local geometric latent embedding \mathbf{h}_j via Eq.1 is then updated using $PE(\mathbf{v}_j)$ from Eq.2, giving:

$$\mathbf{h}_j^{PE} = \phi(\mathbf{h}_j * PE(\mathbf{v}_{rel}) + PE(\mathbf{v}_{rel})), \quad (3)$$

where ϕ represents a learnable function (i.e., shared ResMLPs).

Learnable feature aggregation: aggregation of latent embeddings (i.e., via sum, max and mean functions) are commonly used to update latent node embeddings during graph message-passing in the graph neighbourhood $\mathcal{X}_{\mathcal{K}_i}$:

$$\mathbf{h}_i = \text{aggr}(\mathbf{h}_j^{PE}), \mathbf{h}_i \in \mathcal{H}^l, j \in \mathcal{K}_i, \quad (4)$$

where $\mathcal{H}^l \in \mathbb{R}^{N \times D}$ refers to an aggregated node feature matrix of $\mathcal{G}(\mathcal{M})$ at layer l .

As per Xu et al. (2018), sum aggregation is the most expressive in learning graph structures, whereas mean aggregation performs well when the graph’s statistical distribution needs to be preserved for downstream tasks. Aggregation by max supports learning distinct node features that best represent the neighbourhood, which is of importance in point clouds. Yet, while simple aggregation functions exhibit desirable geometric invariant properties (i.e., permutation invariance and equivariance), they can not effectively aggregate geometric graph features in a generalised feature space, as discussed in Li et al. (2023), causing suboptimal performances in downstream tasks.

Following the definition in Li et al. (2023), we therefore propose a differentiable generalised aggregation function for

local geometric feature aggregation. Specifically, we consider a learnable softmax function:

$$\begin{aligned} \text{aggr}_{\text{softmax}}(\mathbf{h}_j^{PE}; \mathbf{t}) &= \sum_{j \in \mathcal{K}_i} \text{softmax}(\mathbf{h}_j^{PE}; \mathbf{t}) * \mathbf{h}_j^{PE}, \\ \text{softmax}(\mathbf{h}_j^{PE}; \mathbf{t}) &= \frac{\exp(\mathbf{t} * \mathbf{h}_j^{PE})}{\sum_{n \in \mathcal{K}_i} \exp(\mathbf{t} * \mathbf{h}_n^{PE})}, \end{aligned} \quad (5)$$

where \mathbf{t} refers to a differentiable inverse temperature parameter for scaling the randomness of features for softmax input. For $\mathbf{t} \in (-\infty, +\infty)$, the function $\text{aggr}_{\text{softmax}}(\cdot; \mathbf{t} \rightarrow +\infty)$ approximates aggr_{max} ; the function $\text{aggr}_{\text{softmax}}(\cdot; \mathbf{t} \rightarrow -\infty)$ approximates aggr_{min} ; and finally $\text{aggr}_{\text{softmax}}(\cdot; \mathbf{t} = 0)$ approximates $\text{aggr}_{\text{mean}}$. In the differentiable setting, learning the inverse temperature parameter \mathbf{t} of the softmax function allows for aggregating generalised features in a latent space between the aggregated max, min and mean features.

Thus, the learnable generalised aggregation function enables adaptive learning of generalised geometric features (i.e., the representative topology and geometry features specific to the barycentric dual graph $\mathcal{G}(\mathcal{M})$). Here, we consider two types of aggregation: a fixed, non-differentiable simple max and mean aggregations to capture the distinct node features, and the aggregated statistical properties and distribution of node features; and a generalised, differentiable $\text{softmax}(\mathbf{h}_j^{PE}; \mathbf{t} = 1)$ to aggregate the weighted sum of node features. We then add the two types of aggregation:

$$\begin{aligned} \mathbf{h}_i^{\text{aggr}} &= \text{aggr}_{\text{max}}(\mathbf{h}_j^{PE}) \\ &+ \text{aggr}_{\text{mean}}(\mathbf{h}_j^{PE}) \\ &+ \text{aggr}_{\text{softmax}}(\mathbf{h}_j^{PE}; \mathbf{t} = 1.0). \end{aligned} \quad (6)$$

3.4. Hierarchical & Local Pooling

Pooling operations are fundamental building blocks in hierarchical and local information learning of 3D geometry (Zhang et al., 2023). Hierarchical pooling of 3D data is typically implemented by the heuristic farthest Point Sampling (FPS) (Qi et al., 2017b), which commonly applied in 3D point cloud learning with the computational complexity $O(N^2)$ (Hu et al., 2021), or quadric error metric (QEM) simplification (Garland and Heckbert, 1997), which downsamples the 3D geometry of point clouds or mesh vertices while preserving the geometric information. The computational bottleneck of 3D segmentation networks indeed stems from these hierarchical pooling approaches, as confirmed by (Hu et al., 2020).

To improve segmentation efficiency on large-scale landscape surface data, here we apply the random node sub-sampling for hierarchical pooling of the barycentric graph $\mathcal{G}(\mathcal{M})$. However, the random sub-sampling of barycentric graph could randomly drop important nodes that preserve meaningful information of graph (i.e., geometric features). Therefore, we propose to utilise an edge similarity pooling approach to reconstruct and maintain the local graph neighbourhoods of the hierarchically pooled graph of $\mathcal{G}(\mathcal{M})$.

Random node sub-sampling:. In comparison to FPS, random sub-sampling uniformly subsets \mathcal{S} points from \mathcal{N} input points with a computational complexity $\mathcal{O}(1)$. Here we randomly sub-sample \mathcal{S} number of node features from $\mathcal{G}(\mathcal{M})$ at the current layer, giving $\mathcal{H}_S^l = \{h_1, h_2, \dots, h_S\} \in_{\mathcal{R}} \mathcal{H}_N^{l-1}$. We collapse the edges connecting removed nodes and retain only edges connecting the sub-sampled nodes, $\mathcal{E}_{sparse}^l \subseteq \mathcal{H}_S^l \times \mathcal{H}_S^l$. Together the random node sub-sampling operation produces a sparse barycentric graph $\mathcal{G}^l(\mathcal{M}) = (\mathcal{V}_S^l, \mathcal{E}_{sparse}^l)$ with node features \mathcal{H}_S^l .

Edge similarity pooling: a major drawback of random hierarchical pooling is the loss of geodesic relations (i.e., the face adjacency of original mesh \mathcal{M}) in the sparse barycentric graph $\mathcal{G}^l(\mathcal{M})$. Yet, Schult et al. (2020) have empirically demonstrated the benefits of preserving geodesic features in mesh-based learning. They suggested the QEM mesh simplification for the generation of a hierarchy of coarse meshes retaining geodesic information after pooling operations. However, QEM is not directly applicable to barycentric graph settings, and the QEM mesh simplification is not well supported by GPU computations, and therefore inadequate for end-to-end training.

Instead, we propose a heuristic edge similarity pooling method that locally appends new edges to the downsampled barycentric graph containing sparse edge connections. Since the original barycentric graph $\mathcal{G}^0(\mathcal{M})$ has edges \mathcal{E}^0 modelling the face adjacency (i.e., 1-ring neighbours) of input mesh \mathcal{M} , we safely assume for each node in the pooled, sparse barycentric $\mathcal{G}^l(\mathcal{M})$ to have k geodesic neighbours, where $\{k \in \mathbb{Z} : 1 \leq k \leq 3\}$. We then compute $k = 3$ nearest neighbours for each node based on the vertex coordinates $v_i \in \mathcal{V}_S^l$, giving a new edge matrix $\mathcal{E}_{k=3}^l \subseteq \mathcal{H}_S^l \times \mathcal{H}_S^l$. We then update the sparse edges with the newly computed dense edges: $\mathcal{E}_{dense}^l = \mathcal{E}_{sparse}^l + \mathcal{E}_{k=3}^l$. These dense edges might, however, encode redundant Euclidean information from the k nearest neighbour clustering. To better reflect the geodesic relations of the original barycentric graph, we drop redundant edges from the dense edges \mathcal{E}_{dense}^l based on the cosine similarity of node features connected by an edge $(h_i, h_j) \in \mathcal{E}_{dense}^l$:

$$S_C(h_i, h_j) = \frac{h_i \cdot h_j}{\max(\|h_i\|_2, \|h_j\|_2)}. \quad (7)$$

This results in a matrix capturing the similarity of node features in latent space connected by edges in \mathcal{E}_{dense}^l . The redundant edges connecting spatially nearby nodes with low similarity (i.e., a pre-defined threshold value) are dropped, producing a locally geodesic edge matrix \mathcal{E}_{local}^l .

Compared to the dynamic edge pooling approach in Wang et al. (2019), which dynamically recomputes the graph neighbours of 3D point clouds using the k -nearest neighbour clustering in the latent feature space, the proposed heuristic edge similarity pooling computes local k -nearest neighbours in Euclidean space, a more efficient computation with low memory consumption.

Hierarchical & local latent embedding:. We finally compute the k -nearest neighbours ($k=20$) for each $v_i \in \mathcal{V}_S^l$ from the original \mathcal{V}_N^{l-1} , which constitute a hierarchical Euclidean neighbourhood encoded by edge \mathcal{E}_{hier}^l .

With \mathcal{E}_{hier}^l and \mathcal{E}_{local}^l as inputs to the GA+ layer (Sec. 3.3), this results in the Hierarchical Geometry Aggregation (HGA+) and Local Geometry Aggregation (HGA+) layers, respectively capturing hierarchical Euclidean and locally geodesic features of the barycentric graph $\mathcal{G}^l(\mathcal{M})$.

4. Experiments

We conduct experiments on two large-scale landscape surface mesh datasets (Sec. 4.1): SUM (Gao et al., 2021) and the Budj Bim Wall (BBW) dataset, to evaluate the performance of LMSeg on object semantic segmentation task. We compare model performances of LMSeg with existing learning-based segmentation models and report the quantitative and qualitative segmentation results in Sec. 4.4.

4.1. Dataset

SUM (Gao et al., 2021) is a public benchmark dataset of semantic urban meshes (Fig. 3), covering approx. $8km^2$ total captured surface area ($4km^2$ map area, plus objects) in the central region of Helsinki, Finland, classified into six semantic object classes, plus an unclassified complement class. SUM includes 64 tiles: 40 annotated training tiles, 12 validation and 12 test tiles, randomly selected. Each tile covers a $250m^2$ map area with mesh face density of ~ 6.5 faces/ m^2 . The textured mesh tiles in SUM are generated from oblique aerial imagery by triangulation, dense image matching, and mesh surface reconstruction.

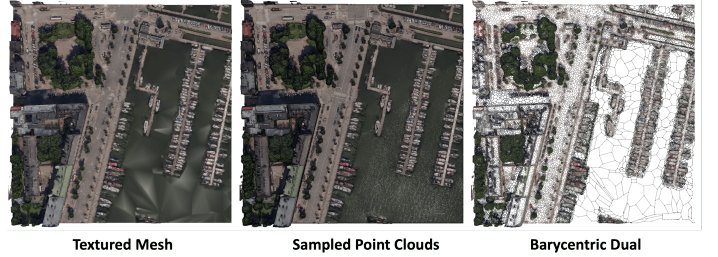


Figure 3: Non-uniformly textured mesh, 3D point cloud and barycentric dual graph of the SUM dataset, respectively. 3D point clouds are densely sampled from the textured mesh in point density of 30 points per mesh surface area (m^2), as recorded in Gao et al. (2021).

BBW dataset is a lidar-scanned point-cloud dataset of the UNESCO World Heritage cultural landscape (Smith et al., 2019; Bell et al., 2019), covered by the Budj Bim National Park in southwest Victoria, Australia (Fig.4). This is one of the areas with the highest density of European historic dry-stone walls in Australia. The dataset was collected in 2020 by the Department of Environment, Land, Water and Planning in Victoria, Australia for the Gunditj Mirring Traditional Owners Corporation.

The BBW dataset is a subset of the full dataset, capturing the northern part of the data. It is spatially divided into six equal, rectangular areas, as shown in Fig.5, where areas 1, 3, 5, 6 are part of the training set (2633 tiles), area 4 is the validation set (716 tiles) and area 2 is the test set (647 tiles). Each tile in BBW dataset is a textured landscape mesh of $400m^2$ map area (with face density of ~ 45 faces/ m^2) semi-manually annotated

into binary semantic labels (wall vs. other terrain). The textured mesh tiles of BBW dataset are constructed from filtered ground surface points resulting from ground/non-ground classification by the data producer. The mesh 2.5D surface is constructed by Delaunay triangulation of the ground surface 3D points. The texture (color information) of the colorized lidar point clouds is projected onto the mesh faces.

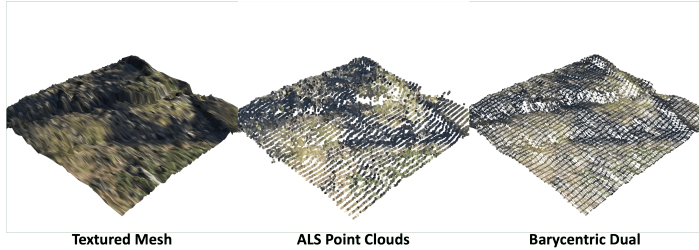


Figure 4: Near-uniform textured triangular mesh, 3D lidar point cloud (ALS) and barycentric dual graph of BBW dataset, respectively.

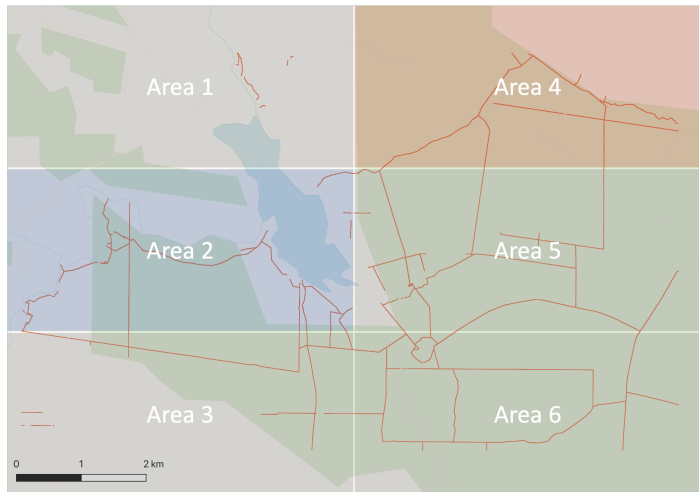


Figure 5: Data splitting of Budj Bim Wall dataset. Train set: Area 1, 3, 5, 6. Validation set: Area 4. Test set: Area 2. Colour annotations denote the spatial locations of European historic dry-stone walls located near Tae Rak (Lake Condah), Victoria, Australia.

4.2. Data Pre-processing

During pre-processing of the landscape mesh data, the primal meshes \mathcal{M} are converted to their barycentric dual graph $\mathcal{G}(\mathcal{M})$. Data (geometric) augmentations are applied to the training data: normalise scale normalise graph node positions to interval $[-1, 1]$; random rotation of each tile around z -axis by random large angles $\in [-180^\circ, 180^\circ]$, around x - and y -axis by random small angles $\in [-1^\circ, 1^\circ]$; random jitter translation of the graph node positions individually within a small interval $\in [-0.001, 0.001]$, post-normalisation. The colour texture information of mesh faces (as HSV values) and face normals are used as barycentric graph node features.

4.3. Implementation

We train LMSeg with an AdamW optimizer (Loshchilov and Hutter, 2017) of weight decay 0.0001 with an initial learning rate of 0.005 for SUM dataset with batch size of 1 and 0.01 for BBW with batch size of 4, respectively. Learning rates were scheduled to decay by the cosine annealing scheduler. We apply a cross entropy, resp. binary loss (for BBW) for supervised multi/binary-class segmentation with the label smoothing technique to effectively prevent over-confident predictions of deep networks. To mitigate the unbalanced semantic-class distribution in datasets, we apply a normalised class weight vector computed from the class distribution of datasets to cross, resp. binary entropy loss. The mean Intersection-over-Union (mIoU) and mean accuracy (mAcc.) metrics are used for model evaluation of multi-class segmentation on SUM dataset. For model evaluation of binary-class segmentation on BBW dataset, we apply the mIoU and F1 score (F1) metrics. All experiments and baselines are implemented in PyTorch Geometric (Fey and Lenssen, 2019) on a Linux server with a NVIDIA A40-24Q GPU.

4.4. Results

Performance on SUM:. Table 1 presents the performance of LM-Seg evaluated on SUM. LMSeg achieves an overall performance of 73.0% mIoU and 79.8% mAcc. on SUM and significantly outperforms all point-based learning methods (Qi et al., 2017a,b; Hu et al., 2020; Thomas et al., 2019), trained on the original 3D point clouds densely sampled from the faces of textured meshes (See Fig.3).

LMSeg also outperforms existing mesh-based learning approaches, RF-MRF (Rouhani et al., 2017) and SUM-RF (Gao et al., 2021), trained on over-segmented surperfacts (i.e., clusters of adjacent mesh faces that share similar characteristics) based on hand-crafted geometric and radiometric mesh features. Comparing to a more recent mesh-based learning approach, the TexturalSG (Yang et al., 2023), which leverages the surface graph of textured meshes as inputs, LMSeg achieves an overall comparable segmentation performance and substantially outperforms TexturalSG on small-object classes (i.e., Vehic. and Boat).

LMseg achieves a highly efficient inference performance on SUM dataset, requiring only ~ 2 minutes (the second-best inference performance after PointNet++) for mesh segmentation on test dataset. We attribute the efficient inference performance of LMSeg to the random node sub-sampling and heuristic edge similarity pooling method proposed in Section 3.4. The point-based method, KPConv, has comparable overall performance (68.8% mIoU and 73.7% mAcc.) as LMSeg, but requires nearly $10\times$ more training parameters and a $14\times$ longer inference time for mesh segmentation.

LMSeg achieves superior performance on four out of six semantic object classes (i.e., H-veg: 93.4%, Build.: 93.3%, Vehic.: 71.9% and Boat: 30.0%) comparing to existing learning-based segmentation methods. Notably, LMSeg outperforms other segmentation methods on small-object class (i.e., Vehic. and Boat) by a large margin, suggesting the geometrical advantages of the graph message-passing GA+ layers and adaptive feature aggregation proposed in Section 3.3. The feature maps of SUM in

Table 1: 3D semantic segmentation results on SUM dataset. Proportions of surface area (per semantic object class) of test set are displayed next to each category in (%). Model results are adopted from the public benchmark SUM (Gao et al., 2021) and approach TexturalSG (Yang et al., 2023). We compare the performance of LMSeg (average performances over five runs) with existing learning-based segmentation methods. Results reported are per-class IoU (%), mean IoU (%), overall accuracy (%) and mean accuracy (%). Model efficiency is evaluated by inference time (minute) on test dataset. Best results marked in bold.

Modality	Method	Terra. (23.6%)	H-veg. (14.3%)	Build. (50.7%)	Water (4.8%)	Vehic. (1.5%)	Boat (2.1%)	mIoU	O.A.	mAcc.	Sampling	Params. (M)	t inf. (Min)
Point Clouds	PointNet (Qi et al., 2017a)	56.3	14.9	66.7	83.8	0.0	0.0	36.9 ± 2.3	71.4 ± 2.1	46.1 ± 2.6	-	3.6	1
	RandLANet (Hu et al., 2020)	38.9	59.6	81.5	27.7	22.0	2.1	38.6 ± 4.6	74.9 ± 3.2	53.3 ± 5.1	Random	1.3	52
	SPG (Landrieu and Simonovsky, 2018)	56.4	61.8	87.4	36.5	34.4	6.2	47.1 ± 2.4	79.0 ± 2.8	64.8 ± 1.2	-	-	26
	PointNet++ (Qi et al., 2017b)	68.0	73.1	84.2	69.9	0.5	1.7	49.5 ± 2.1	85.5 ± 0.9	57.8 ± 1.8	FPS	1.0	3
	KPCConv (Thomas et al., 2019)	86.5	88.4	92.7	77.7	54.3	13.3	68.8 ± 5.7	93.3 ± 1.5	73.7 ± 5.4	FPS	15.0	42
Mesh	RF-MRF (Rouhani et al., 2017)	77.4	87.5	91.3	83.7	23.8	1.7	60.9 ± 0.0	91.2 ± 0.0	65.9 ± 0.0	-	-	15
	SUM-RF (Gao et al., 2021)	83.3	90.5	92.5	86.0	37.3	7.4	66.2 ± 0.0	93.0 ± 0.0	70.6 ± 0.0	-	-	18
	TexturalSG (Yang et al., 2023)	88.2	91.0	92.9	90.1	47.6	18.9	71.5 ± 1.9	94.1 ± 1.2	-	Random	-	-
	LMSeg (Ours-avg)	81.4	93.4	93.3	68.2	71.9	30.0	73.0 ± 0.03	94.0 ± 0.07	79.8 ± 0.06	Random	1.7	2

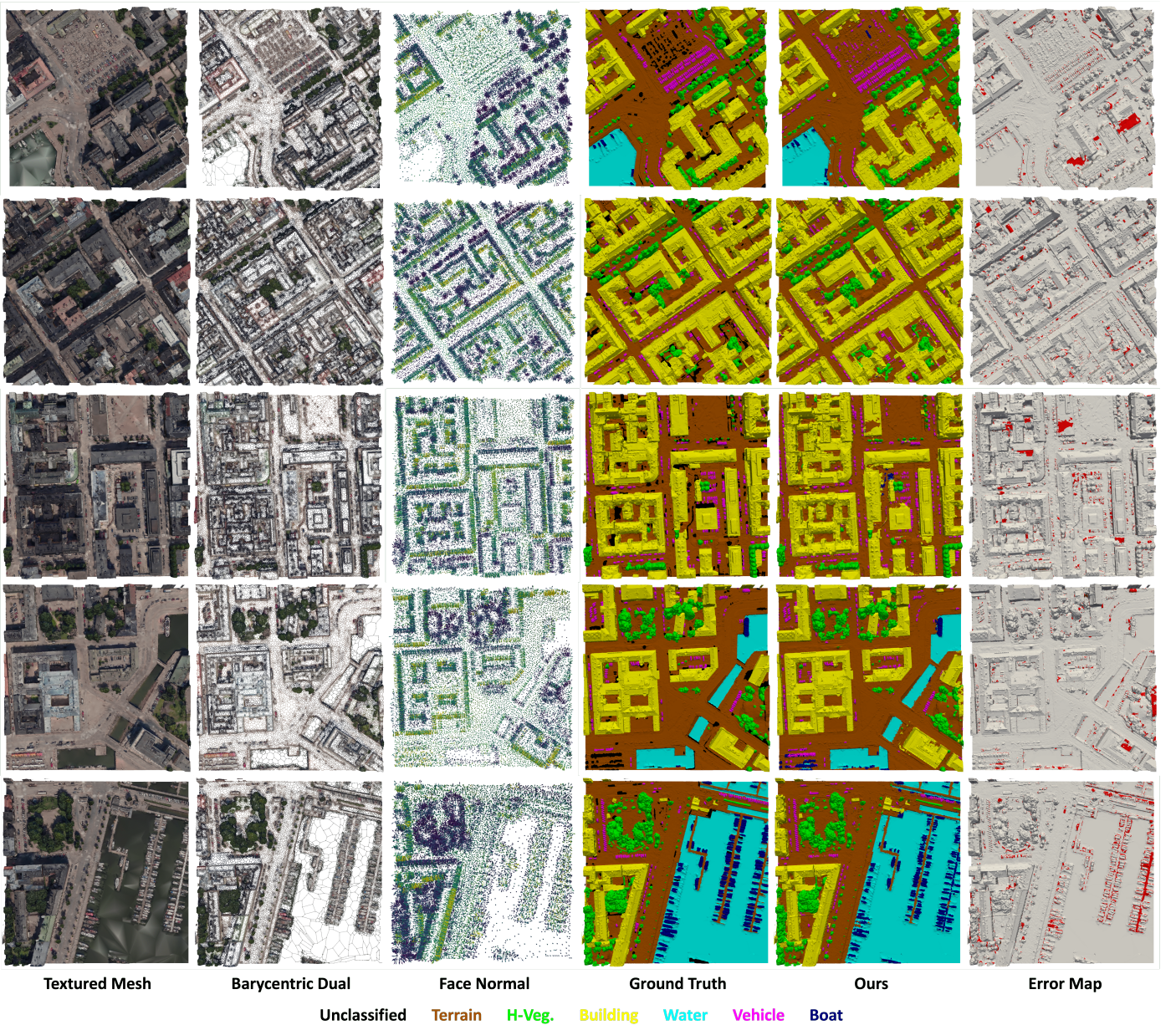


Figure 6: Qualitative performance of LMSeg on SUM dataset.

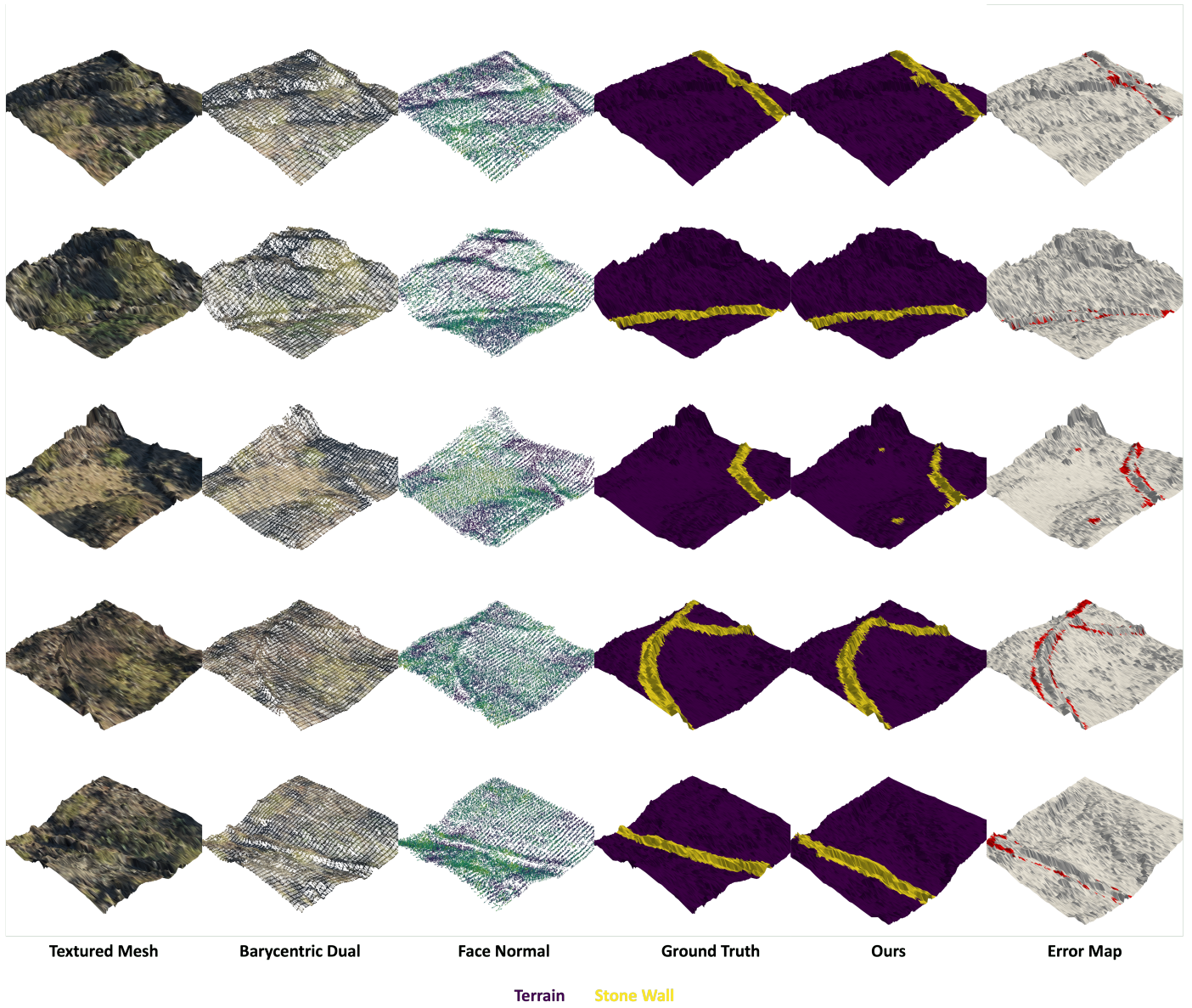
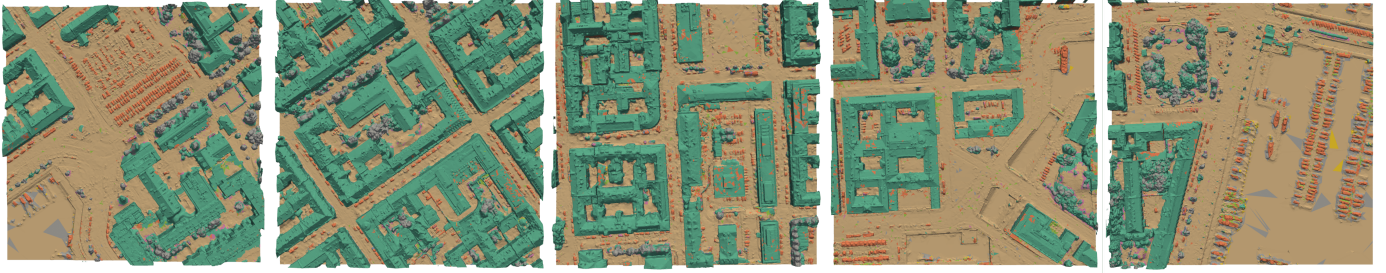
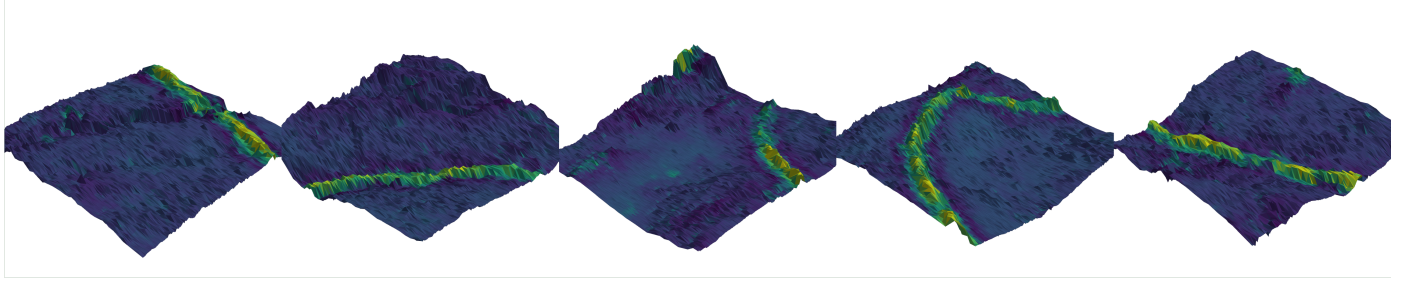


Figure 7: Qualitative performance of LMSeg on BBW dataset.



(a) Feature maps visualised for SUM dataset, where different colors of surfaces mapping to over-segmented surfaces.



(b) Feature maps visualised for BBW dataset, where lighter colors indicate stronger feature responses.

Figure 8: Feature maps of final feature propagation layer of LMSeg (Fig. 1) on SUM (top) and BBW (bottom) datasets.

Table 2: 3D semantic segmentation results on BBW dataset. Proportions of surface area (per semantic object class) of test set: Wall (11.4%) vs. Terra. (88.5%). Performance reported is mean IoU (%) and F1 score (%). Model efficiency is evaluated by inference time (second) on test and validation sets. We present the model performance on validation (Area 4 - Top) and test (Area 2 - Bottom) set. Best results marked in bold.

Method	F1	mIoU	Sampling	Params. (M)	t inf. (Sec.)
RandLANet (Hu et al., 2020)	66.4	50.4	Random	1.3	24.2
PointNet++ (Qi et al., 2017b)	60.1	42.9	FPS	1.0	42.7
PointTransformer (Zhao et al., 2021)	59.7	42.6	FPS	5.0	92.2
DeeperGCNs (Li et al., 2023)	48.3	32.8	-	1.9	47.8
Graph U-Net (Gao and Ji, 2019)	39.7	25.1	Top k	0.85	44.2
LMSeg (Ours)	74.0	58.5	Random	1.7	27.3
RandLANet (Hu et al., 2020)	69.8	53.7	Random	1.3	22.8
PointNet++ (Qi et al., 2017b)	60.3	43.3	FPS	1.0	42.3
PointTransformer (Zhao et al., 2021)	64.5	47.5	FPS	5.0	90.1
DeeperGCNs (Li et al., 2023)	51.6	35.5	-	1.9	46.8
Graph U-Net (Gao and Ji, 2019)	43.0	28.9	Top k	0.85	44.7
LMSeg (Ours)	74.6	59.5	Random	1.7	27.7

Fig. 8(a) further show that LMSeg can effectively learn strong latent embeddings for large (i.e., Build. and H-veg.) and small non-planar objects (i.e., Vehic. and Boat) in large-scale urban landscapes.

The qualitative results of LMSeg tested on SUM are presented through error maps in Fig. 6. Prediction errors occur mostly at the boundary of two connected objects in ambiguous regions (i.e., ground surfaces adjacent to boats and water surface, as shown in row 5, Fig. 6). These ambiguous regions likely cover areas with common labelling errors in triangle mesh annotations, as discussed extensively in (Gao et al., 2021). Other errors happen on segmentation between ground and water surfaces (i.e., Water and Terra. classes), sharing geometrically similar barycentric graph structures but cover un-even portions of the surface area of SUM classes (i.e., Terra. class (23.6%) vs. Water class (4.8%)).

Performance on BBW: We present LMSeg validation results (on Area 4) and test results (on Area 2) in Table 2 and the qualitative performance in Fig. 7. For comparison, we include different point-based learning methods (i.e., RandLANet (Hu et al., 2020), PointNet++ (Qi et al., 2017b) and Point Transformer (Zhao et al., 2021)) and graph-based learning methods (i.e., DeeperGCNs (Li et al., 2023) and Graph U-Net (Gao and Ji, 2019)), ensuring comparable model sizes and training parameters. In practice, the graph-based methods take the barycentric graph of the processed landscape mesh as inputs and the point-based methods take the vertex points of the barycentric graph as inputs. Overall, LMSeg achieves the best mIoU of 59.5% and 58.5%, F1 score of 74.6% and 74.0% among all methods on test (Area 2) and validation (Area 4) sets.

Natural landscape meshes in BBW, unlike urban landscape meshes in SUM, have dense, uniformly distributed triangles

capturing fine-grained geometric objects (i.e., walls and ditches) of the terrain surface. Point-based learning methods (i.e., RandLANet (Hu et al., 2020): 50.4% and 53.7% mIoU, Point Transformer (Zhao et al., 2021): 42.6% and 47.5% mIoU, PointNet++ (Qi et al., 2017b): 42.9% and 43.3% mIoU) perform generally better than graph-based learning methods with deep residual graph convolution networks (i.e., DeeperGCNs (Li et al., 2023): 32.8% and 35.5% mIoU and Graph U-Net (Gao and Ji, 2019): 25.1% and 28.9 mIoU) operating on the barycentric graph of meshes.

Comparing to point-based methods (Qi et al., 2017b; Hu et al., 2020; Zhao et al., 2021) that commonly leverage relative point positions to learn local geometric features of 3D point clouds in local neighbourhoods (Eq. 1) and apply simple aggregations (i.e., max or mean function) for local geometric aggregation, LMSeg’s GA+ layers more effectively capture strong and salient geometric features (i.e., slopes uprising from planar surfaces and terrains) and adaptively aggregate latent geometric features from local neighbours via the proposed learnable aggregation layers (Eq. 6). The feature maps of BBW in Fig. 8(b) visualise the strong feature response (light color) on the locations of irregular stone wall structures compared to the weak feature response (dark color) on terrains in natural landscapes.

Comparing to graph-based methods (i.e., DeeperGCNs with very deep 28-ResGCN layers, and Graph U-Net with hierarchical graph structure learning via graph convolution layers and Topk node sub-sampling), LMSeg’s HGA+ and LGA+ layers have the benefits of learning hierarchical and local geometric features of barycentric graphs, leading to a more efficient and accurate model performance.

Error maps of LMSeg on the BBW dataset (Fig. 4) show prediction errors mainly at ambiguous boundaries between irregular stone walls and the terrain, likely due to misclassified labels from human annotators.

Table 3: List of ablated models tested in the Ablation study.

Ablated Model	Description
SUM-A	Without HGA+ components.
SUM-B	Without LGA+ components.
SUM-C	Without learnable feature aggregation.
SUM-D and E	With 8- and 12-nearest neighbours.
SUM-F	Without SUM HSV colour.
SUM-G	Without SUM face normals.
BBW-A and B	Tested on 75%-res. meshes.
BBW-C and D	Tested on 50%-res. meshes.
BBW-E and F	Tested on 30%-res. meshes.
BBW-G and H	Without BBW HSV colour.
BBW-I and J	Without BBW face normals.

5. Discussion

We conduct a series of ablation studies of LMseg on the SUM and BBW datasets (Table 3) and present the results of the ablated models in Table 4 and 5, respectively, to gain an

in-depth understanding and identify the effective components of the model.

Effect of HGA+ and LGA+. Removing either HGA+ or LGA+ components from the LMSeg architecture triggers performance deterioration (LMSeg mIoU drop: 73.0% \rightarrow SUM-A: 57.7% and SUM-B: 70.4%, Table 4). Removing the HGA+ components (SUM-A) from LMSeg significantly lowers the model’s segmentation performance on all object classes. The decrease in performance caused by removing LGA+ (SUM-B) from LMSeg impacts the Water and small-object classes (i.e., Vehic.: 71.9% \rightarrow 68.0%, Boat: 30.0% \rightarrow 27.3% and Water: 68.2% \rightarrow 63.0%). The ablation study of HGA+ and LGA+ components of LMSeg confirms the importance of learning hierarchical and local geometric features for landscape mesh segmentation, in particular for the segmentation of small-object classes.

Effect of learnable feature aggregation. SUM-C (Table 4) tests the effect of learnable feature aggregation in GA+ layers of LMSeg on landscape mesh segmentation. SUM-C removes the proposed adaptive aggregation in HGA+ and LGA+ modules (Eq. 6) and applies only the simple aggregations (i.e., max and mean function), as commonly applied in point-based learning methods (Qi et al., 2017b; Hu et al., 2020; Zhao et al., 2021). We observe that SUM-C with vanilla-GA layers (i.e., HGA and LGA) leads to reduced performance (LMSeg mIoU: 73.0% \rightarrow SUM-C: 68.9%) across object classes (except for Boat) with the most severe mIoU deterioration on Water and Vehic. classes (Water: 68.2% \rightarrow 58.7%, Vehic.: 71.9% \rightarrow 61.5%).

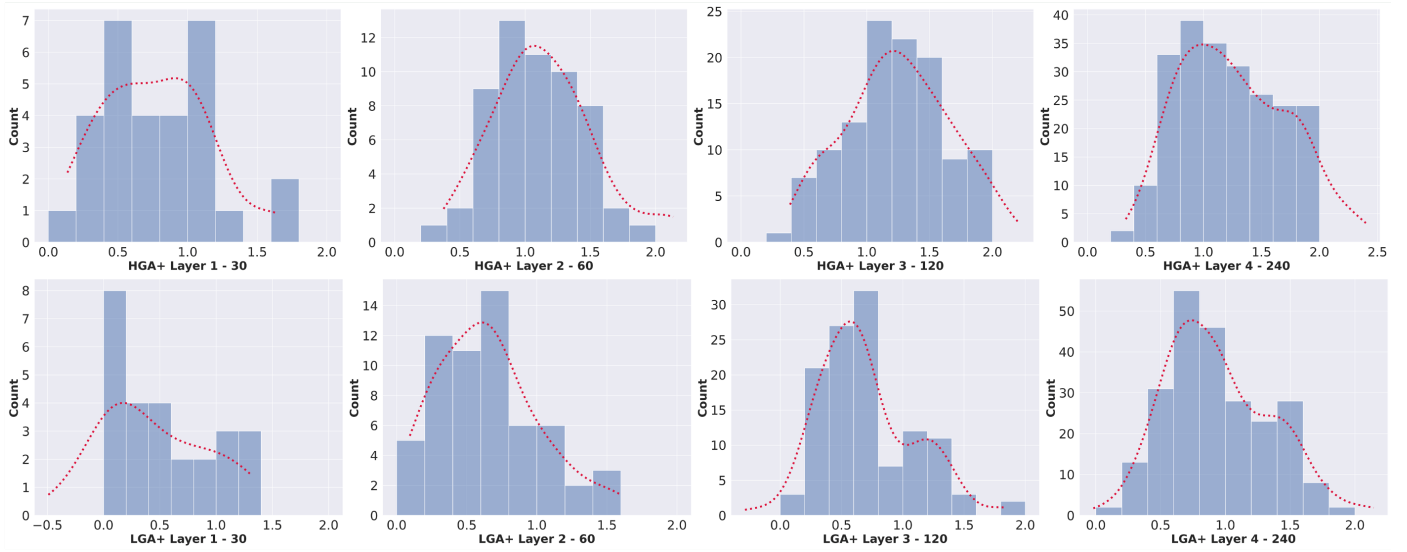
We further delve into the effect of learnable feature aggregation by visualising the weight vector distributions of inverse temperature t (all-one vectors to instantiate softmax aggregation) of learnable aggregation layers (Fig. 9). Fig. 9(a)-(b) show that the learnable aggregation layers trained on SUM and BBW datasets enable adaptive aggregation of latent geometric features. This is the effect of approximation of generalised aggregate functions by the learning of inverse temperature t (Li et al., 2023): $aggr_{\text{mean}} = aggr_{\text{softmax}}(\cdot; \mathbf{t} = 0)$, $aggr_{\text{min}} = aggr_{\text{softmax}}(\cdot; \mathbf{t} \rightarrow -\infty)$ and $aggr_{\text{max}} = aggr_{\text{softmax}}(\cdot; \mathbf{t} \rightarrow +\infty)$. The quantitative results of ablated SUM-C and the visualisation of weight vector distributions of inverse temperature t collectively demonstrate the effectiveness and advantage of learnable aggregation layers for landscape mesh segmentation over simple aggregations (Qi et al., 2017b; Hu et al., 2020; Zhao et al., 2021).

Effect of local nearest neighbours. SUM-D and E examine the effect of k -nearest neighbors in HGA+ layers on model performance. Results show that reducing k leads to fluctuating mIoU: 73.0% (LMSeg, $k = 16$) \rightarrow 73.1% (SUM-D, $k = 12$) and 68.1% (SUM-E, $k = 8$). Therefore, k is a tunable hyper-parameter for the target mesh dataset. Increasing k can potentially capture richer geometric information on hierarchical sub-sampled barycentric graph $\mathcal{G}^{l-1}(\mathcal{M}) \rightarrow \mathcal{G}^l(\mathcal{M})$ for better performance but at a higher computational cost.

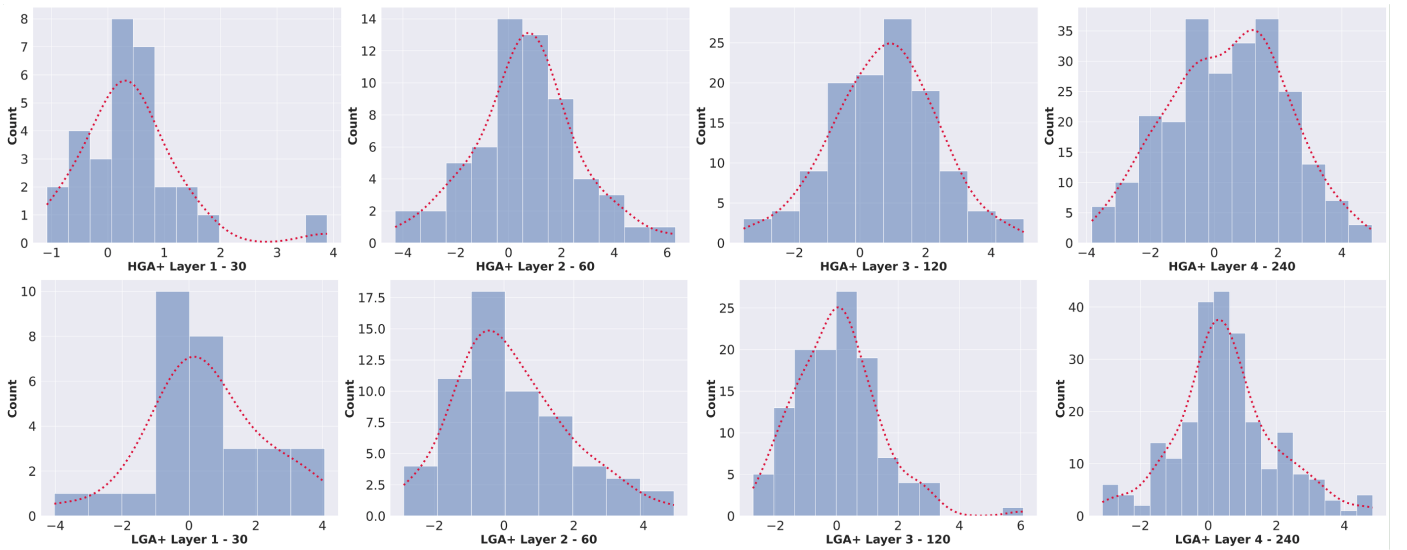
Effect of mesh resolution. We investigated LMSeg’s performance on natural landscape meshes at 75%, 50%, and 30% res-

Table 4: Ablation study of LMSeg on SUM dataset. Δ refers to the performance (mIoU) difference of ablated models compared to LMSeg.

Model	k -nbrs.	Encoder	Terra.	H-veg.	Build.	Water	Vehic.	Boat	mIoU	Δ
SUM-A	3*	LGA+	73.7	90.4	91.2	33.2	50.6	6.8	57.7	-15.3
SUM-B	16	HGA+	78.9	92.4	92.5	63.0	68.0	27.3	70.4	-2.6
SUM-C	16 (3*)	HGA & LGA	77.7	92.4	92.6	58.7	61.5	30.7	68.9	-4.1
SUM-D	8 (3*)	HGA+ & LGA+	77.9	92.3	92.2	58.4	61.7	26.1	68.1	-4.9
SUM-E	12 (3*)	HGA+ & LGA+	81.7	93.6	93.3	69.2	70.9	29.6	73.1	+0.1
SUM-F	16 (3*)	HGA+ & LGA+	71.0	65.8	82.6	40.1	58.0	25.9	57.2	-15.8
SUM-G	16 (3*)	HGA+ & LGA+	79.0	93.1	92.5	68.4	68.7	29.3	71.9	-1.1
LMSeg (Ours-avg)	16 (3*)	HGA+ & LGA+	81.4	93.4	93.3	68.2	71.9	30.0	73.0	-



(a) SUM dataset.



(b) BBW dataset.

Figure 9: The weight vector distributions of inverse temperature t on SUM and BBW dataset. Weights are initialised to ones to instantiate softmax aggregation.

Table 5: Ablation study of LMSeg on BBW dataset. Δ refers to the performance (mIoU) difference of ablated models compared to LMSeg performance on evaluation (Area 4 - Top) and test (Area 2 - Bottom) set. Mesh resolution is the ratio of face numbers of simplified mesh to original mesh.

Model	Mesh Res. (%)	F1	mIoU	Δ
BBW-A	75.0	74.3	59.1	+0.6
BBW-C	50.0	69.8	53.4	-5.1
BBW-E	30.0	54.0	37.4	-21.1
BBW-G	100.0	70.7	54.7	-3.8
BBW-I	100.0	73.6	58.3	-0.2
LMSeg (Ours)	100.0	74.0	58.5	-
BBW-B	75.0	75.1	60.6	+1.1
BBW-D	50.0	71.8	56.3	-3.2
BBW-F	30.0	59.1	42.2	-17.3
BBW-H	100.0	72.1	56.4	-3.1
BBW-J	100.0	74.5	59.4	-0.1
LMSeg (Ours)	100.0	74.6	59.5	-

olutions of the BBW dataset (Table 5). The meshes were simplified via QEM simplification to coarser resolutions and converted to barycentric graphs for input. At 75% resolution, models BBW-A (58.5% \rightarrow 59.1% on Area 4) and BBW-E (59.5% \rightarrow 60.6% on Area 2) showed slight mIoU improvements. At 50% resolution, models BBW-B (58.5% \rightarrow 53.4% on Area 4) and BBW-F (59.5% \rightarrow 56.3% on Area 2) suffered minor mIoU degradation. At 30% resolution, models BBW-C (58.5% \rightarrow 37.4% on Area 4) and BBW-G (59.5% \rightarrow 42.2% on Area 2) experienced significant mIoU degradation. These results demonstrate LMSeg’s robustness across varying landscape resolutions.

Effect of mesh features: LMSeg has been tested with with face normals and HSV colour features \mathcal{X} appended to nodes \mathcal{V} of the barycentric graph $\mathcal{G}(\mathcal{M})$.

Models SUM-F and SUM-G (Table 3) test the impact of HSV colour and face normals, respectively, on SUM dataset. The result of ablated SUM-G on Table 4 indicates that the face normals have a mild impact on model performance, decreasing mIoU by 1.1% (73.0% \rightarrow 71.9%). In contrast, the removal of HSV color features (i.e., ablated SUM-F) significantly degrades mIoU by 15.8% (73.0% \rightarrow 57.2%) across object classes, indicating that HSV color is crucial for distinguishing objects (i.e., H-veg., Water and Vehic.) in urban landscapes.

Models BBW-G, H, and BBW-I, J (Table 3) assessed the impact of HSV color and face normals on the BBW validation and test sets. Removing HSV color features (i.e., BBW-G and H) resulted in relatively small performance drops (58.5% \rightarrow 54.7% on Area 4 and 59.5% \rightarrow 56.4% on Area 2). The removal of face normals (i.e., BBW-I and J) showed negligible changes (58.5% \rightarrow 58.3% on Area 4 and 59.5% \rightarrow 59.4% on Area 2). This is likely because the geometric features (face normals) of terrain and wall classes are similar, and the semantic information of stone walls is affected by bush/tree objects, as shown in Fig. 7, making these features less effective for segmentation.

6. Conclusions

In this study, we introduce LMSeg, an efficient deep graph message-passing network for accurate semantic segmentation of large-scale 3D landscape meshes. LMSeg utilizes barycentric dual graphs of landscape meshes, enabling end-to-end model training with deep graph message-passing networks. It leverages geometric and texture features of triangular surface meshes (face normals and color information) for accurate segmentation, learning hierarchical and local geometric features through Geometry Aggregation Plus (GA+) layers.

Our results on large-scale urban and natural landscape datasets show that LMSeg outperforms existing mesh segmentation methods in accuracy and inference efficiency, with notable improvements in segmenting small mesh objects (i.e., Vehic. and Boat in SUM) and irregular stone wall structures.

However, LMSeg shows lower performance on mesh objects with geometrically similar barycentric graph structures (e.g., Water and Terra. in SUM) due to limited network receptive fields. Future research will focus on developing a network capable of learning finer semantic mesh features and capturing comprehensive global spatial information with a larger receptive field.

CRediT authorship contribution statement

Zexian Huang: Conceptualization, Writing – original draft, Writing – review & editing, Software, Methodology, Investigation. **Kourosh Khoshelham:** Writing – review & editing, Supervision. **Gunditj Mirring Traditional Owners Corporation:** Supervision. **Martin Tomko:** Writing – review & editing, Supervision.

Declaration of Competing Interest

The authors declare that they have no known competing financial interests or personal relationships that could have appeared to influence the work reported in this paper.

Data availability

The source code and data support the findings of this study are available in figshare.com with the anonymous link: <https://figshare.com/s/046d7cf4576c75ed0571>.

Acknowledgements

We thank Gunditj Mirring Traditional Owners Corporation (GMTOC) for providing the research data and overseeing its usage in this study, as well as Mashnoon Islam for his dedicated data annotation work; their invaluable cooperation, support, and meticulous efforts have significantly contributed to the quality of our research.

References

- Adam, J.M., Liu, W., Zang, Y., Afzal, M.K., Bello, S.A., Muhammad, A.U., Wang, C., Li, J., 2023. Deep learning-based semantic segmentation of urban-scale 3d meshes in remote sensing: A survey. *International Journal of Applied Earth Observation and Geoinformation* 121, 103365.
- Bell, D., Molloy, L., Prpic, J., Tomko, M., 2019. A new world heritage site for aboriginal engineering. *Nature* 572, 32–33.
- Blaschke, T., 2010. Object based image analysis for remote sensing. *ISPRS journal of photogrammetry and remote sensing* 65, 2–16.
- Bronstein, A.M., Bronstein, M.M., Guibas, L.J., Ovsjanikov, M., 2011. Shape google: Geometric words and expressions for invariant shape retrieval. *ACM Transactions on Graphics (TOG)* 30, 1–20.
- Dosovitskiy, A., Beyer, L., Kolesnikov, A., Weissenborn, D., Zhai, X., Unterthiner, T., Dehghani, M., Minderer, M., Heigold, G., Gelly, S., et al., 2020. An image is worth 16x16 words: Transformers for image recognition at scale, in: *International Conference on Learning Representations*.
- Feng, Y., Feng, Y., You, H., Zhao, X., Gao, Y., 2019. Meshnet: Mesh neural network for 3d shape representation, in: *Proceedings of the AAAI conference on artificial intelligence*, pp. 8279–8286.
- Fey, M., Lenssen, J.E., 2019. Fast graph representation learning with pytorch geometric. *arXiv preprint arXiv:1903.02428*.
- Gao, H., Ji, S., 2019. Graph u-nets, in: *international conference on machine learning*, PMLR. pp. 2083–2092.
- Gao, W., Nan, L., Boom, B., Ledoux, H., 2021. Sum: A benchmark dataset of semantic urban meshes. *ISPRS Journal of Photogrammetry and Remote Sensing* 179, 108–120.
- Garland, M., Heckbert, P.S., 1997. Surface simplification using quadric error metrics, in: *Proceedings of the 24th annual conference on Computer graphics and interactive techniques*, pp. 209–216.
- Gilmer, J., Schoenholz, S.S., Riley, P.F., Vinyals, O., Dahl, G.E., 2017. Neural message passing for quantum chemistry, in: *International conference on machine learning*, PMLR. pp. 1263–1272.
- Girshick, R., Donahue, J., Darrell, T., Malik, J., 2014. Rich feature hierarchies for accurate object detection and semantic segmentation, in: *Proceedings of the IEEE conference on computer vision and pattern recognition*, pp. 580–587.
- Guan, B., Li, H., Zhou, F., Lin, S., Wang, R., 2021. Lgcnpnet: local-global combined point-based network for shape segmentation. *Computers & Graphics* 97, 208–216.
- Hanocka, R., Hertz, A., Fish, N., Giryas, R., Fleishman, S., Cohen-Or, D., 2019. Meshcn: a network with an edge. *ACM Transactions on Graphics (ToG)* 38, 1–12.
- He, K., Zhang, X., Ren, S., Sun, J., 2016. Deep residual learning for image recognition, in: *Proceedings of the IEEE conference on computer vision and pattern recognition*, pp. 770–778.
- Hu, Q., Yang, B., Xie, L., Rosa, S., Guo, Y., Wang, Z., Trigoni, N., Markham, A., 2020. Randa-net: Efficient semantic segmentation of large-scale point clouds, in: *Proceedings of the IEEE/CVF conference on computer vision and pattern recognition*, pp. 11108–11117.
- Hu, Q., Yang, B., Xie, L., Rosa, S., Guo, Y., Wang, Z., Trigoni, N., Markham, A., 2021. Learning semantic segmentation of large-scale point clouds with random sampling. *IEEE Transactions on Pattern Analysis and Machine Intelligence* 44, 8338–8354.
- Kipf, T.N., Welling, M., 2017. Semi-supervised classification with graph convolutional networks, in: *5th International Conference on Learning Representations, ICLR 2017, Toulon, France, April 24–26, 2017, Conference Track Proceedings, OpenReview.net*. URL: <https://openreview.net/forum?id=SJU4ayYg1>.
- Kölle, M., Laupheimer, D., Schmohl, S., Haala, N., Rottensteiner, F., Wegner, J.D., Ledoux, H., 2021. The hessigheim 3d (h3d) benchmark on semantic segmentation of high-resolution 3d point clouds and textured meshes from uav lidar and multi-view-stereo. *ISPRS Open Journal of Photogrammetry and Remote Sensing* 1, 100001.
- Landrieu, L., Simonovsky, M., 2018. Large-scale point cloud semantic segmentation with superpoint graphs, in: *Proceedings of the IEEE conference on computer vision and pattern recognition*, pp. 4558–4567.
- Laupheimer, D., Shams Eddin, M., Haala, N., 2020. On the association of lidar point clouds and textured meshes for multi-modal semantic segmentation. *ISPRS Annals of the Photogrammetry, Remote Sensing and Spatial Information Sciences* 2, 509–516.
- Li, G., Muller, M., Thabet, A., Ghanem, B., 2019. Deepgcns: Can gcns go as deep as cnns?, in: *Proceedings of the IEEE/CVF international conference on computer vision*, pp. 9267–9276.
- Li, G., Xiong, C., Qian, G., Thabet, A., Ghanem, B., 2023. Deepergcn: training deeper gcns with generalized aggregation functions. *IEEE Transactions on Pattern Analysis and Machine Intelligence*.
- Loshchilov, I., Hutter, F., 2017. Decoupled weight decay regularization. *arXiv preprint arXiv:1711.05101*.
- Ma, X., Qin, C., You, H., Ran, H., Fu, Y., 2022. Rethinking network design and local geometry in point cloud: A simple residual mlp framework. *arXiv preprint arXiv:2202.07123*.
- Milano, F., Loquercio, A., Rosinol, A., Scaramuzza, D., Carlone, L., 2020. Primal-dual mesh convolutional neural networks. *Advances in Neural Information Processing Systems* 33, 952–963.
- Peucker, T.K., Fowler, R.J., Little, J.J., Mark, D.M., COLUMBIA)*, S.T.D.L.V.B., 1976. Digital representation of three-dimensional surfaces by Triangulated Irregular Networks (TIN)(Revised). Simon Fraser University, Burnaby, British Columbia, Canada and Office of Naval Research, Geography Programs, Arlington, Virginia, USA, Technical Report No 10.
- Qi, C.R., Su, H., Mo, K., Guibas, L.J., 2017a. Pointnet: Deep learning on point sets for 3d classification and segmentation, in: *Proceedings of the IEEE conference on computer vision and pattern recognition*, pp. 652–660.
- Qi, C.R., Yi, L., Su, H., Guibas, L.J., 2017b. Pointnet++: Deep hierarchical feature learning on point sets in a metric space. *Advances in neural information processing systems* 30.
- Qian, G., Li, Y., Peng, H., Mai, J., Hammoud, H., Elhoseiny, M., Ghanem, B., 2022. Pointnext: Revisiting pointnet++ with improved training and scaling strategies. *Advances in Neural Information Processing Systems* 35, 23192–23204.
- Rouhani, M., Lafarge, F., Alliez, P., 2017. Semantic segmentation of 3d textured meshes for urban scene analysis. *ISPRS Journal of Photogrammetry and Remote Sensing* 123, 124–139.
- Schult, J., Engelmann, F., Kontogianni, T., Leibe, B., 2020. Dualconvmesh-net:

- Joint geodesic and euclidean convolutions on 3d meshes, in: Proceedings of the IEEE/CVF Conference on Computer Vision and Pattern Recognition, pp. 8612–8622.
- Singh, V.V., Sheshappanavar, S.V., Kambhamettu, C., 2021. Meshnet++: A network with a face., in: ACM Multimedia, pp. 4883–4891.
- Smith, A., McNiven, I.J., Rose, D., Brown, S., Johnston, C., Crocker, S., 2019. Indigenous knowledge and resource management as world heritage values: Budj bim cultural landscape, australia. *Archaeologies* 15, 285–313.
- Tailor, S.A., de Jong, R., Azevedo, T., Mattina, M., Maji, P., 2021. Towards efficient point cloud graph neural networks through architectural simplification, in: Proceedings of the IEEE/CVF International Conference on Computer Vision, pp. 2095–2104.
- Tancik, M., Srinivasan, P., Mildenhall, B., Fridovich-Keil, S., Raghavan, N., Singhal, U., Ramamoorthi, R., Barron, J., Ng, R., 2020. Fourier features let networks learn high frequency functions in low dimensional domains. *Advances in Neural Information Processing Systems* 33, 7537–7547.
- Tang, R., Xia, M., Yang, Y., Zhang, C., 2022. A deep-learning model for semantic segmentation of meshes from uav oblique images. *International Journal of Remote Sensing* 43, 4774–4792.
- Tang, W., Qiu, G., 2021. Dense graph convolutional neural networks on 3d meshes for 3d object segmentation and classification. *Image and Vision Computing* 114, 104265.
- Thomas, H., Qi, C.R., Deschaud, J.E., Marcotegui, B., Goulette, F., Guibas, L.J., 2019. Kpconv: Flexible and deformable convolution for point clouds, in: Proceedings of the IEEE/CVF international conference on computer vision, pp. 6411–6420.
- Tutzauer, P., Laupheimer, D., Haala, N., 2019. Semantic urban mesh enhancement utilizing a hybrid model. *ISPRS Annals of the Photogrammetry, Remote Sensing and Spatial Information Sciences* 4, 175–182.
- Vaswani, A., Shazeer, N., Parmar, N., Uszkoreit, J., Jones, L., Gomez, A.N., Kaiser, Ł., Polosukhin, I., 2017. Attention is all you need. *Advances in neural information processing systems* 30.
- Wang, L., Li, R., Zhang, C., Fang, S., Duan, C., Meng, X., Atkinson, P.M., 2022. Unetformer: A unet-like transformer for efficient semantic segmentation of remote sensing urban scene imagery. *ISPRS Journal of Photogrammetry and Remote Sensing* 190, 196–214.
- Wang, Y., Sun, Y., Liu, Z., Sarma, S.E., Bronstein, M.M., Solomon, J.M., 2019. Dynamic graph cnn for learning on point clouds. *ACM Transactions on Graphics (tog)* 38, 1–12.
- Weixiao, G., Nan, L., Boom, B., Ledoux, H., 2023. Pssnet: Planarity-sensible semantic segmentation of large-scale urban meshes. *ISPRS Journal of Photogrammetry and Remote Sensing* 196, 32–44.
- Wu, Z., Song, S., Khosla, A., Yu, F., Zhang, L., Tang, X., Xiao, J., 2015. 3d shapenets: A deep representation for volumetric shapes, in: Proceedings of the IEEE conference on computer vision and pattern recognition, pp. 1912–1920.
- Xu, K., Hu, W., Leskovec, J., Jegelka, S., 2018. How powerful are graph neural networks? *arXiv preprint arXiv:1810.00826*.
- Yang, Y., Tang, R., Xia, M., Zhang, C., 2023. A surface graph based deep learning framework for large-scale urban mesh semantic segmentation. *International Journal of Applied Earth Observation and Geoinformation* 119, 103322.
- Zhang, R., Wang, L., Wang, Y., Gao, P., Li, H., Shi, J., 2023. Parameter is not all you need: Starting from non-parametric networks for 3d point cloud analysis. *arXiv preprint arXiv:2303.08134*.
- Zhao, H., Jiang, L., Jia, J., Torr, P.H., Koltun, V., 2021. Point transformer, in: Proceedings of the IEEE/CVF international conference on computer vision, pp. 16259–16268.